How Robot Dogs See the Unseeable



Fig. 1. Animal and robotic peering enhance scene understanding under limited vision. Using side-to-side peering motions, insects like katydids (e.g., bush crickets) and locusts leverage motion parallax to perceive depth beyond what stereoscopic vision provides. Similarly, robots with limited aperture optics (e.g., the ANYbotics ANYmal) can use this strategy to suppress partial occlusion. While sophisticated vision reasoning of large multimodal models (here, ChatGPT-5.0) struggles to interpret occluded scenes when being asked to interpret visible content in conventional images, these models show improved understanding once occlusion is suppressed through peering in synthetic aperture (SA) integral imagery. Robot peering suppresses occlusion in real-time and is wavelength-independent, as demonstrated in the visible (RGB) and near-infrared (NIR) examples above. For the RGB example, a peering motion (=SA) of approximately 11cm was used to sample and integrate 300 images captured with a wide-angle lens. For the NIR example, the peering motion was approx. 7cm and integrated 27 images captured with a standard lens. The physical aperture of both cameras was 0.965mm (f/2). See Movie S1 in supplementary materials.

Authors:

Oliver Bimber^{1*}, Karl Dietrich von Ellenrieder², Michael Haller³, Rakesh John Amala Arokia Nathan¹, Gianni Lunardi², Marco Camurri⁴, Mohamed Youssef¹, Santos Miguel Orozco Soto², Jeremy E. Niven⁵

Affiliations:

¹Department of Computer Science, Johannes Kepler University Linz, Austria

One Sentence Summary: (92/125 characters)

By mimicking how insects peer side-to-side, robots can now see through clutter in real-time.

²Field Robotics Laboratory South Tyrol, Free University of Bozen-Bolzano, Italy

³Media Interaction Lab, Free University of Bozen-Bolzano, Italy

⁴Department of Industrial Engineering, University of Trento, Italy

⁵School of Life Sciences, University of Sussex, UK

^{*}Corresponding author. Email: oliver.bimber@jku.at

Main Text: (988/1000 words)

Peering is the characteristic side-to-side body movement animals use to judge distance before jumping or striking. Animals with limited, short range stereovision exploit motion parallax with movements that create relative motion between nearby and distant objects. The peering of insects, such as praying mantis¹, horse-head grasshoppers², locusts³, or crickets⁴, is well studied. In locusts, for instance, leg movements pivot the body around the abdomen, producing a lateral head displacement that is compensated by an opposite head rotation to stabilize eye orientation³. Such behaviour patterns increase motion parallax. Whether peering serves functions beyond distance estimation (for instance, to see prey through partially occluding foliage) remains unexplored.

Peering quadrupedal robots can see through partially occluding ground vegetation and other obstacles. Potential applications are manifold and range from surveillance, terrain exploration, inspection, search-and-rescue, and more. This work establishes a connection between peering in visual perception and synthetic aperture sensing in optical imaging. We show that this principle improves scene understanding not only in animals but also in robots.

In optical imaging, cameras integrate light through the aperture of their lenses. The depth of field is the distance range, measured along the optical axis, on either side of the focal plane within which objects will appear acceptably sharp in an image. The small (e.g., less than a millimeter wide) optical apertures in conventional robot cameras create a fundamental limitation: their large depth of field renders both near and far objects in sharp focus. Consequently, any obstacle in the foreground can obscure objects of interest in the background (Fig. S1 in supplementary materials). Synthetic aperture sensing⁵ is an advanced signal processing technique where a moving sensor (like a radar antenna or optical camera) collects a series of measurements over time and location. These measurements are then computationally combined to synthesize the effect of a single, much larger aperture. During peering, the robot's camera-equipped head describes a (several centimeter wide) synthetic aperture (SA) in which hundreds of images and corresponding poses are recorded. These images are computationally integrated to produce an image with the extremely shallow depth of field that a physical lens of the SA's size would create⁶. A synthetic focal surface, such as a plane, cylinder, sphere, or more complex topologies can now be aligned to focus on scenery beyond the occluding foreground. The optical signal of occluders are then lost in the defocus blur, while the optical signal of the focused background is amplified. The computational process, which requires only the projection and averaging of the captured images onto the synthetic focal surface (Fig. S2 in supplementary materials), is efficient enough for real-time operation on mobile processors. It is also wavelength-independent, delivering robust performance across all spectral bands –including visible (RGB), thermal (FIR), near-infrared (NIR), RedEdge (REG), and low-light spectra- making it versatile across numerous applications. The efficacy of synthetic aperture sensing for occlusion removal is highest at 50% occlusion, but degrades with increasing occlusion density.

Animal peering is primarily used to enhance scene understanding with a limited visual system. For estimating depth from motion parallax with compound eyes that support only limited stereo vision, a horizontal peering motion is sufficient. Applying this bio-inspired analogy to robots for occlusion suppression also leads to superior scene comprehension, as we will show later, but might require more complex peering patterns. Synthetic aperture sensing with a horizontal sampling pattern, for instance, struggles to suppress large horizontal occluders, as they obscure the background from many viewpoints. Our initial experiments (Fig. S3 and Movie S2 in supplementary materials) show that lateral shift motions yield superior results to axial rotations, as they maximize motion parallax. Furthermore, motions with a vertical component can also suppress horizontally aligned occluders. Partial occlusion has been shown to hinder basic scene understanding tasks, such as classification, and that performance is restored after acalusion removal.

and that performance is restored after occlusion removal^{8,9}. We empirically demonstrate that even the sophisticated visual reasoning capabilities of large multimodal models (LLMs) are unable to interpret occluded backgrounds properly in conventional images, but show successful understanding

when presented with SA integral images where occlusion has been suppressed (Fig. 1 and Fig. S4 in supplementary materials).

Alternative approaches, such as current multi-view 3D vision methods, including model-based structure-from-motion, or deep-learning-based neural radiance fields and visual geometry grounded transformers, suffer from two major limitations. First, their reliance on identifiable image features makes them highly susceptible to occlusions, as they break down when features are hidden (see Fig. S5 in supplementary materials). Second, multi-view techniques require relatively long computations on high-end GPUs. Active sensors like LiDAR and radar can overcome occlusion but suffer from drawbacks such as low spatial resolution, a lack of multispectral data (e.g., color, temperature), and, for adequate resolutions, longer processing times for tasks like pulse compression and point-cloud registration. Peering enables real-time and high-resolution perception (which is essential for vision-based scene understanding) that is low-cost and immediately deployable on any camera-equipped robot. Sensor fusion can further improve these results. For instance, coarse depth data can detect large occluders that are close, while multispectral imaging can identify occluding vegetation using vegetation indices¹⁰. Masking these occluders in the input images before integration suppresses the residual out-of-focus blur in the SA integral imagery (see Fig. S6 in supplementary materials).

The ability to peer is not limited to quadrupedal robots. It is also applicable to bipedal, hexapod, wheeled, or crawling platforms. The peering motion can be achieved either by moving a camera payload, by moving the robot's entire frame (e.g., during navigation), or both. However, replacing this motion with a static array of camera sensors would severely undersample the SA signal and prevent adaptive sampling in response to local occlusion conditions. Further research should explore optimal peering motions, the integration of omnidirectional and multi-spectral vision, and leveraging the resulting motion parallax to break camouflage. These capabilities can be learned by studying evolved animal behaviour. This creates a bidirectional exchange where robotics research and animal behaviour studies can stimulate and build upon one another.

References:

- 1. K. Kral, Side-to-side head movements to obtain motion depth cues: A short review of research on the praying mantis. *Behav. Process.* **43(1)**, 71-77 (1998). https://doi.org/10.1016/S0376-6357(98)00007-2
- 2. J. E. Niven, S. R. Ott, S. M. Rogers, Visually targeted reaching in horse-head grasshoppers. *Proc. R. Soc. B.* **279**, 3697–3705 (2012). https://doi.org/doi:10.1098/rspb.2012.0918
- 3. T. S. Collett, Peering A locust behaviour pattern for obtaining motion parallax information. *J. Exp. Biol.* **76**, 237-241 (1978).
- 4. M. goulet, R. campan, M. lambin, The visual perception of relative distances in the wood-cricket, Nemobius sylvestris. *Physiol. Entomol.* **6(4)**, 357–367 (1981). https://doi.org/10.1111/j.1365-3032.1981.tb00651.x
- 5. P. Vouras, K.V. Mishra, A. Artusio-Glimpse, S. Pinilla, A. Xenaki, D. W. Griffith, K. Egiazarian, An overview of advances in signal processing techniques for classical and quantum wideband synthetic apertures. *IEEE J. Sel. Top. Signal Process.* 17, 317–369 (2023). https://doi.org/10.1109/JSTSP.2023.3262443
- 6. I. Kurmi, D. C. Schedl, O. Bimber, Airborne optical sectioning. *J. Imaging* **4**, 102 (2018). https://doi.org/doi:10.3390/jimaging4080102
- 7. I. Kurmi, D. C. Schedl, O. Bimber, A statistical view on synthetic aperture imaging for occlusion removal. *IEEE Sens. J.* **19**, 9374 9383 (2019). https://doi.org/doi:10.1109/JSEN.2019.2922731
- 8. D. C. Schedl, I. Kurmi, O. Bimber, Search and rescue with airborne optical sectioning. *Nat. Mach. Intell.* **2**, 783–790 (2020). https://doi.org/10.1038/s42256-020-00261-3
- 9. D. C. Schedl, I. Kurmi, O. Bimber, Autonomous Drones for Search and Rescue in Forests, *Sci. Robot.* **6(55)**, eabg1188 (2021). https://doi.org/10.1126/scirobotics.abg1188

10. J. Xue, B. Su, Significant Remote Sensing Vegetation Indices: A Review of Developments and Applications. *J. Sens.* **2017**,1353691 (2017). https://doi.org/10.1155/2017/1353691

Acknowledgements: We thank Stephen M. Rogers (University of Oxford) for assistance with recording katydid peering. Katydid videos were recorded at the University of Cambridge. We thank Armando Castillo (INDICASAT AIP) for assistance recording locust peering.

Funding:

Austrian Science Fund (FWF)/German Research Foundation (DFG) grants I 6046-N P "Wide Synthetic Aperture Sampling for Motion Classification" and 32185-NBL "Wide Synthetic Aperture Sampling" (OB), Cohesion Italy 21-27 Project EFRE1079 "Forest Robotic Monitoring and Automation (FORMA)" CUP I53C24001750006 Cofunded by the EU and the Autonomous Province of Bolzano (KDvE).

Author contributions:

Conceptualization: OB Methodology: OB

Software: RJAAN, GL, MC

Investigation/Implementation: OB, KDvE, MH, RJAAN, GL, MC, MY, SMOS, JEN

Resources: KDvE, OB, JEN, MH

Visualization: OB, RJAAN, GL, MH, MY, JEN

Funding acquisition: OB, KDvE, MH Project administration: OB, KDvE, MH

Supervision: OB, KDvE, MH Writing – original draft: OB

Writing – review & editing: OB, KDvE, MH

Competing interests:

Authors declare that they have no competing interests.

Data and materials availability:

All data are available in the main text or the supplementary materials.

Supplementary Materials

Supplementary Figures

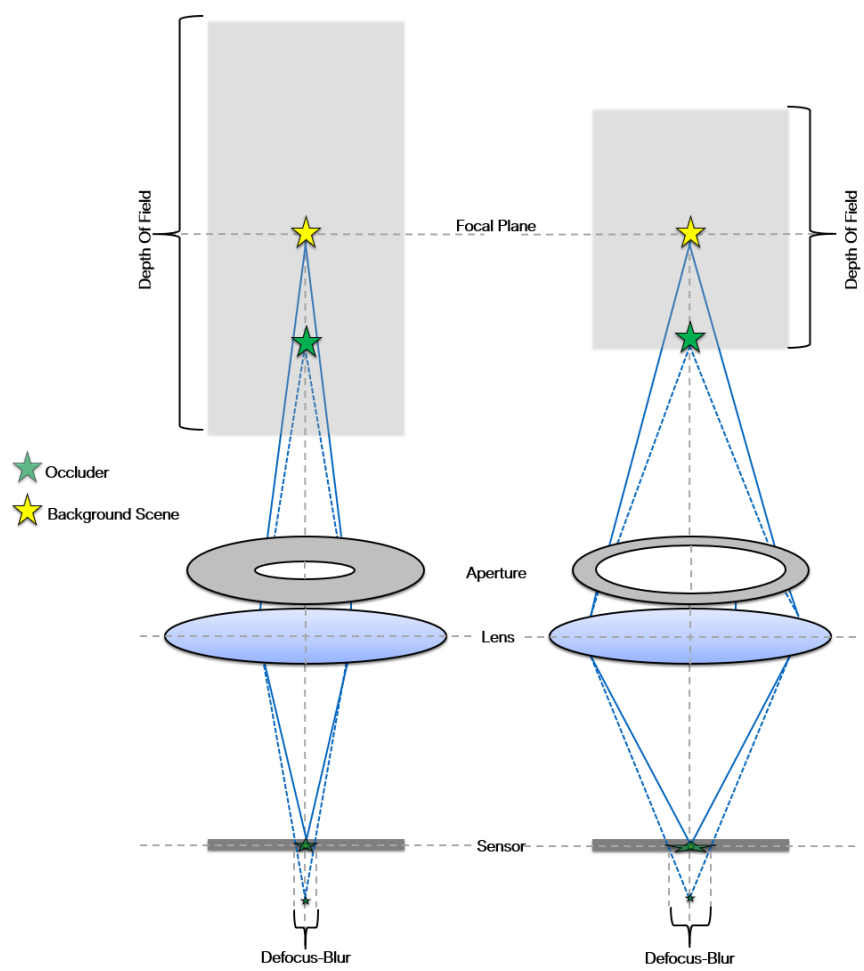


Fig. S1. Depth of field decreases as the aperture widens. A narrow aperture (left) produces minimal defocus blur from out-of-focus objects, resulting in a wide depth of field where both foreground and background appear sharp. Conversely, a wide aperture (right) admits more light but shrinks the depth of field, blurring anything outside the focal plane more. However, conventional camera optics limit the maximum aperture size based on the lens and sensor dimensions. Consequently, robots often use fixed focal-length cameras with sub-millimeter apertures, which keep the entire scene in sharp focus, making the background scene and occluders in the foreground appear equally defined.



Fig. S2. Synthetic aperture sensing via peering motion. The peering motion of a robot (left) enables the capture of hundreds of images using a conventional narrowaperture camera. The trajectory of this motion defines a large synthetic aperture (SA). To synthesize this aperture, the images are projected onto a synthetic focal surface and averaged (right), a process that requires precise camera pose data from the robot's external sensors. The resulting SA, which can be several centimeters wide, creates an extremely shallow depth of field SA integral image. Only the regions near the synthetic focal surface remain in sharp focus, while all other areas are rapidly blurred. We employ a parametric focal surface that can be manipulated in all three dimensions (scaled, translated, and rotated) and can take on various shapes, from a plane to a cylinder, or sphere. Focusing is achieved manually by first selecting a focus point (distance and position) in the viewing direction of the robot, and then transforming and warping the focal surface relative to it. These focus changes are displayed in real-time. Alternatively, the focal surface parameters could be determined automatically using image-based metrics¹¹, similar to a conventional autofocus system. The examples on the right compare a planar and a cylindrical synthetic focal surface. The cylindrical surface provides superior focus on scene elements located at varying distances. The remaining focus blur is caused by objects that are not precisely on the focal surface, combined with inaccuracies in pose estimation.

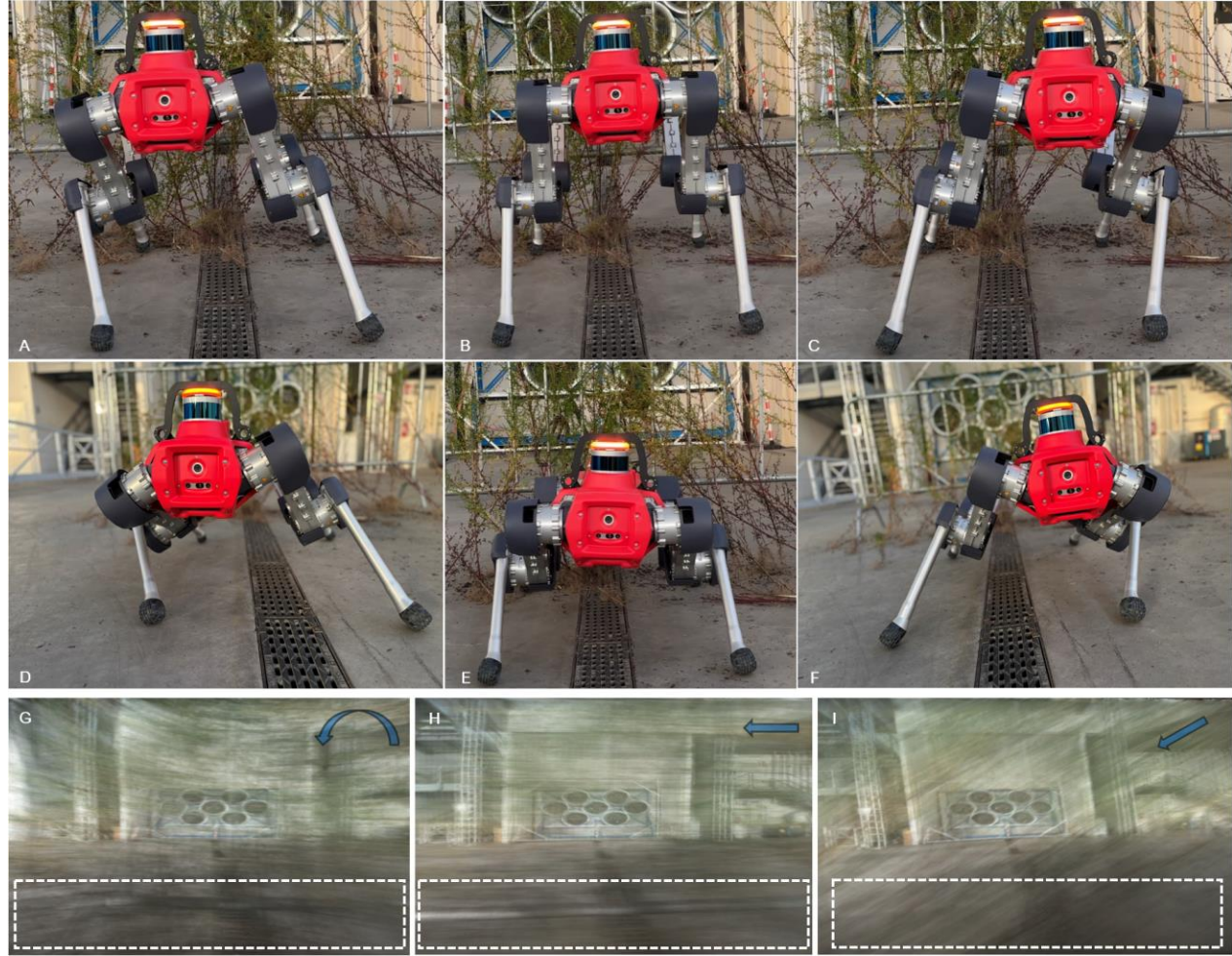


Fig. S3. Peering as lateral shift. Peering can also involve lateral shifts, as opposed to the axial rotation shown in Fig. 1 of the main text. In this case, the camera translates horizontally or vertically while remaining on the same plane, resulting in a planar SA peering motion. This configuration maximizes motion parallax. Note that insects, such as locusts, follow the same objective, compensating for abdomen rotation with an opposite head rotation³. However, since rotating a robot's head is not always feasible, a lateral shift must be used instead. The range of these shifts is constrained by the robot's mechanical limits (for the ANYbotics ANYmal, this was 30cm horizontally and 20cm vertically, A-F). We compare three distinct peering motions (bottom row): a rotational motion (G), as shown in Fig. 1 for reference, using a 15 cm SA with 26 integrated images; a horizontal shift (H) with a 15 cm SA and 20 images; and a diagonal shift with a 16 cm SA and 28 images. The horizontal shift yields superior results to the rotation by maximizing parallax. Furthermore, unlike the purely horizontal motion, the diagonal shift can also suppress horizontally aligned occluders better (such as the fence's metal bar in the dotted box) because it benefits from both horizontal and vertical motion parallax. These examples also demonstrate that effective occlusion removal is achievable with an order of magnitude fewer samples, supporting the use of fast motions even with limited camera frame rates. See Movie S2 in supplementary materials.

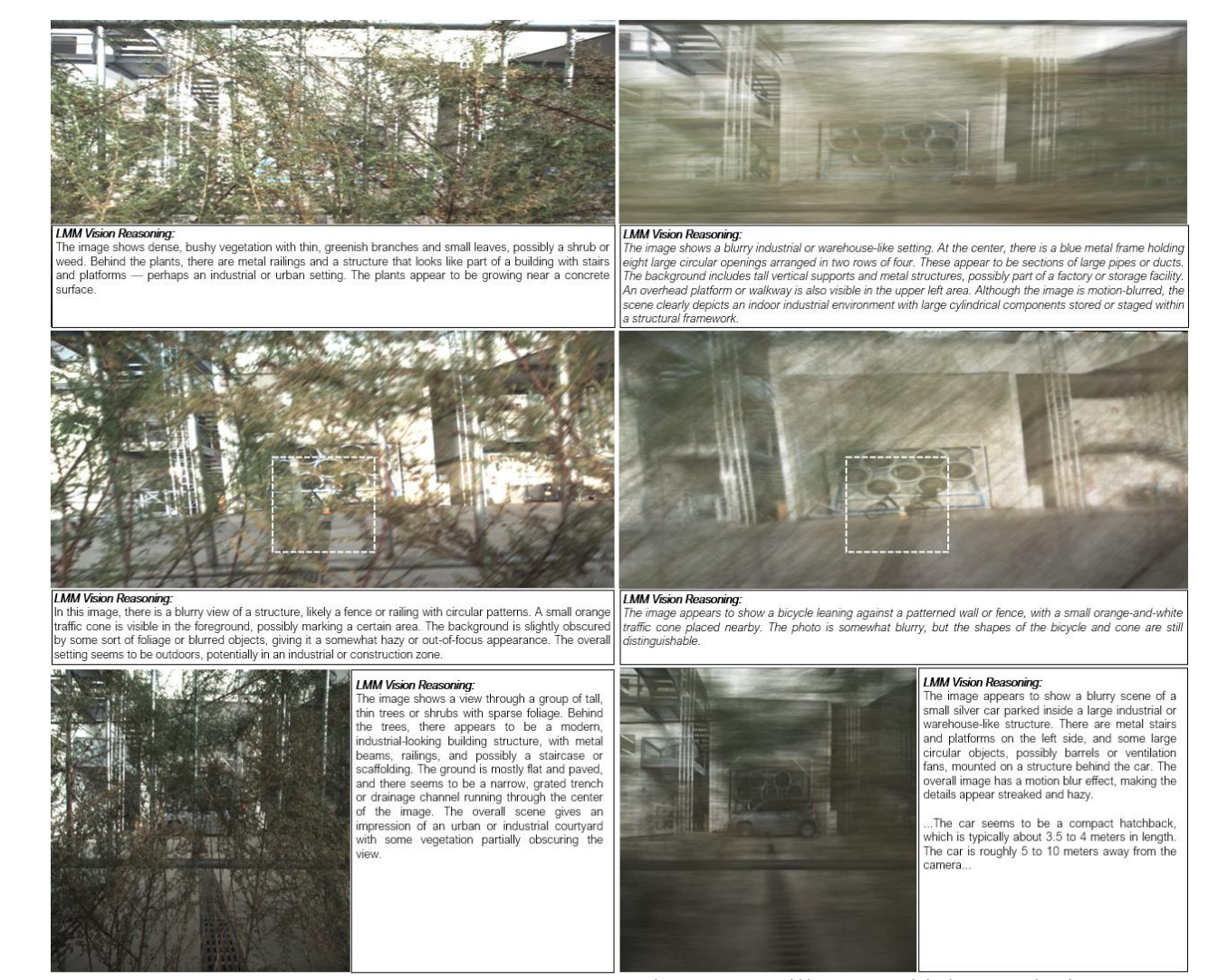


Fig. S4. Additional vision reasoning examples. The top row illustrates higher occlusion density captured with a horizontal shift peering motion (82 images over 12cm). The center row employed a diagonal shift peering motion (32 images over 19cm) with vision reasoning applied on the region of interest (dashed box). The bottom row shows the results from a second horizontal shift peering motion (151 images over 9cm), where distances were also estimated using vision reasoning. All rows present conventional images (left) alongside their SA integral images (right). Note that vision-based reasoning models are non-deterministic 10. Querying the same image content multiple times yields slightly varying responses. For the examples above and in Fig. 1, we used the prompts "What is visible in the image?" and (for the bottom row) "How far is the car away?" with ChatGPT-5.0. The car was approximately 5 meters from the robot.

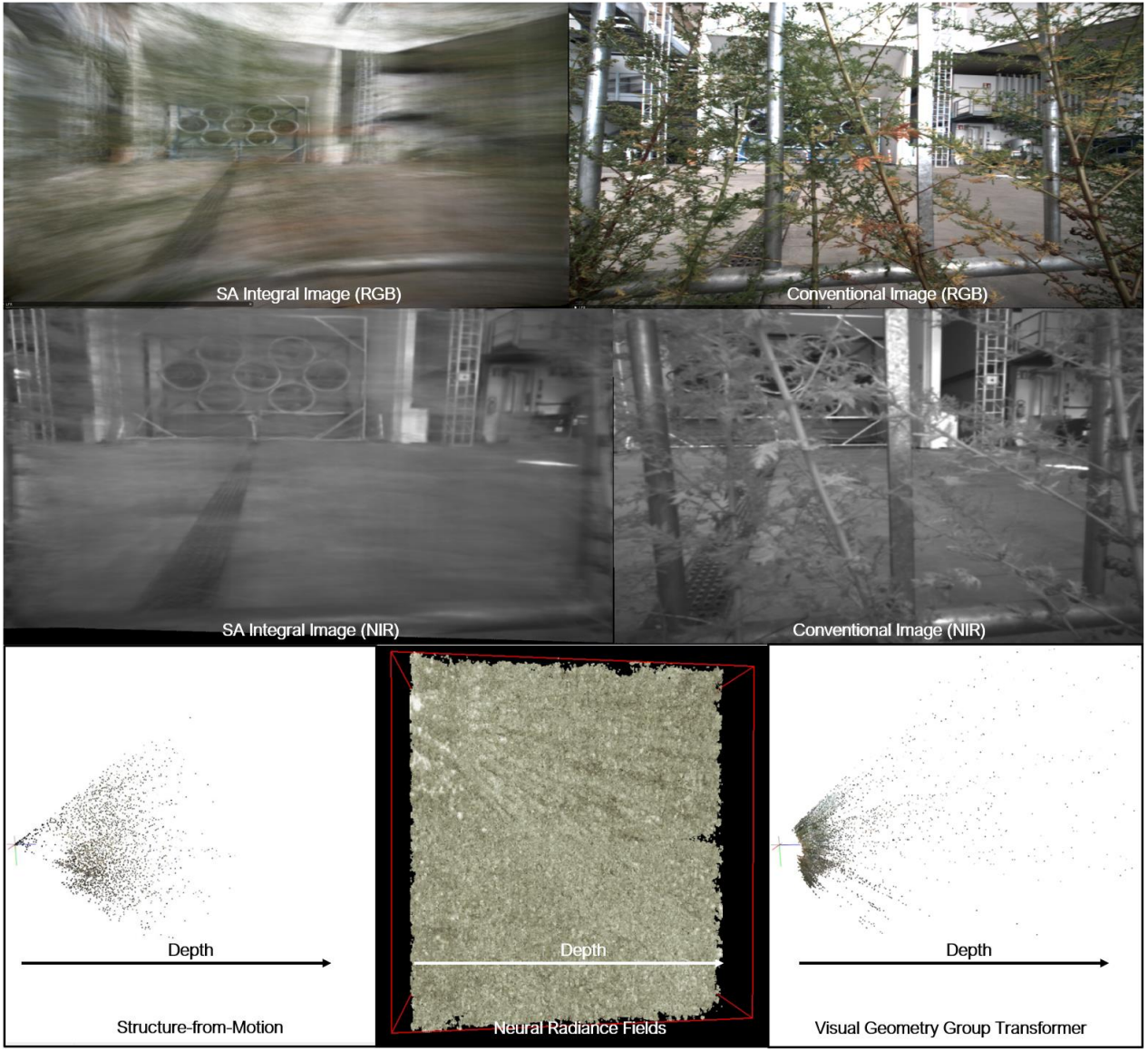


Fig. S5. Synthetic aperture sensing vs 3D vision. Unlike 3D vision techniques, synthetic aperture sensing does not reconstruct depth but instead suppresses partial occlusion in 2D images. Its advantages include real-time performance and wavelength independence. The examples above show the same scene in wide-angle RGB (top) and standard near-infrared, or NIR (center). For comparison, we fed the 300 RGB images recorded from peering into state-of-the-art 3D vision approaches: Structure-from-Motion (SfM)¹², Neural Radiance Fields (NeRF)¹³, and Visual Geometry Group Transformers (VGGT)¹⁴. The SfM and VGGT methods only reconstructed a sparse point cloud of mainly the foreground occluders. The NeRF model produced a volume of widely incoherent noise. All these approaches are not real-time capable (SfM and NERF: approx. 5-6 hours, VGGT: approx. 15 minutes on a high-end GPU) and failed due to severely and randomly occluded features present in the multi-view input.

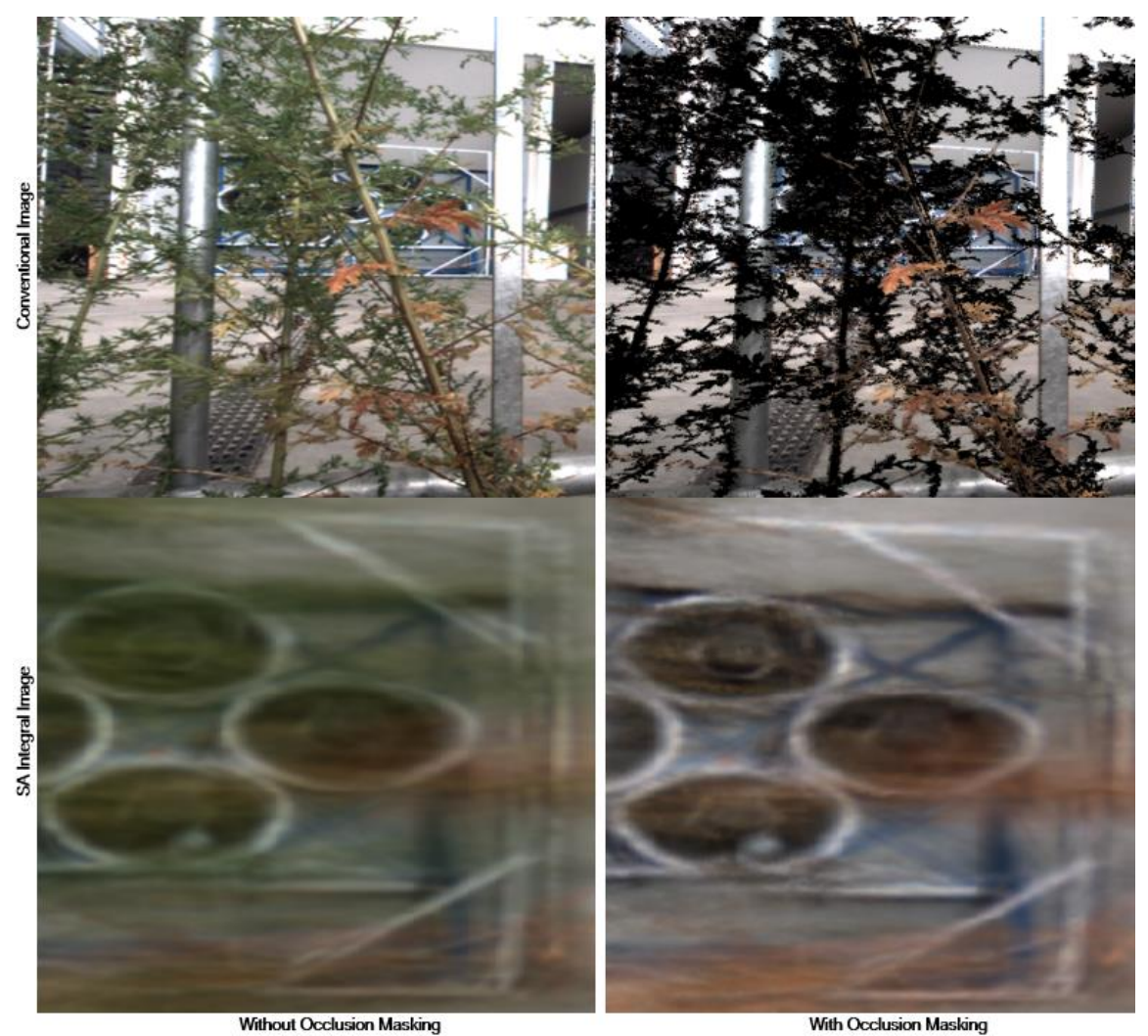


Fig. S6. Occlusion masking for enhanced contrast. Simply averaging all overlapping pixels projected onto the synthetic focal surface (Fig. S2) results in a residual defocus blur from occluders in the final synthetic aperture integral image (left). To suppress this blur and achieve higher contrast, we can employ occlusion masking (right). This technique involves initially identifying potential occluders and averaging only the pixels of non-occluders. The source for an occlusion mask can vary. In the example above, we assume all occluders are plants and use the Visible Difference Vegetation Index (VDVI)¹⁵ to identify and mask likely vegetation pixels. Vegetation indices are often more accurately estimated using spectral bands beyond visible light, a task for which multi-spectral cameras are better suited than standard RGB cameras. Beyond reflectance-based methods, other cues like preliminary depth estimates or thermal radiance could also be used to generate occlusion masks.

Supplementary Movies

Movie S1. Animal and robotic peering enhance scene understanding under limited vision. This movie supplements Fig. 1 in the main text, illustrating dynamic peering motions from locusts, the Florida bush cricket, and ANYbotics' ANYmal robot. It also shows the corresponding images from the robot's perspective during peering, along with the manual focusing process within the synthetic aperture (SA) integral images (here, using a planar synthetic focal surface). Finally, it presents visual reasoning results from a large multimodal model (specifically, ChatGPT-5.0) for both indoor RGB and outdoor near-infrared (NIR) recordings.

Movie S2. Various robotic peering motions. This video demonstrates the peering motions implemented on a quadruped robot, including horizontal rotation, horizontal shift, and diagonal shift. These movements are constrained by the robot's equilibrium limits (avoid falling into the ground). For the ANYbotics ANYmal, this yields a maximum vertical SA of approximately 20cm and a horizontal SA of 30cm in our experiments.

Supplementary Software

The following software is available at: https://doi.org/10.5281/zenodo.17646110



Software S1. Synthetic Aperture Integrator. This software was used to compute the SA integral images from a given set of conventional input images and the corresponding recording poses. It allows adjusting the focal surface (Fig. S2) interactively and supports occlusion masking (Fig. S6) based on Visible the Difference Vegetation Index (VDVI)¹⁵. It requires Microsoft Windows and a reasonably fast GPU. Please note that the following instructions describe only the functionality for viewing the supplementary data. For more detailed information, please contact the corresponding author. To begin, choose a supplementary dataset and copy the *images* and *poses* folders, along with the *parameters.txt* file, into the main *SAI*

directory. By default, the dense scene shown in Fig. S4 is preinstalled. Then, run SAI.exe. Please be aware that loading may take some time, depending on the number of images. Navigate the *Virtual Camera* using the mouse wheel and left button. Within the menu, you can adjust the Focal Surface parameters. The surface can be shifted into the scene using the z-parameter, where a positive value moves it forward. Additionally, it can be translated (TX, TY), rotated (RX, RY, RZ), and scaled (SX, SY, RZ)SZ). Note that the focal surface is based on a unit half-sphere. By selecting large values for SX and SY, the surface will approximate a flat plane, while a positive SZ value scales it in the +z direction. Besides planes, cylindrical and spherical focal surfaces can also be created by setting appropriate values for SX, SY, and SZ. The grid-flag toggles the focal surface grid visualization on or off; the center of this grid indicates the current focus point. To view the individual captured images, select the pinhole aperture option in the Virtual Camera tab and use the Jump to +/- buttons to browse the sequence. To return to the synthetic aperture integration view, simply click the open aperture option. The occlusion mask parameters (T,UB,LB) threshold the occlusion mask values (ranging from -1 to 1). Within this range, high values identify occluder pixels, while low values identify non-occluder pixels. The threshold T serves as the central value for this separation. Pixels with values recognized as occluders are assigned low alpha values, potentially becoming fully transparent (0), whereas non-occluders are assigned high alpha values, potentially becoming fully opaque (1). The LB and UB parameters define lower and upper bounds around T to create a smooth transition. A pixel value below LB is assigned an alpha of 1, and a value above UB is assigned an alpha of 0. For values falling between LB and UB, the alpha value is linearly interpolated between 0 and 1. This entire process is applied to each image individually, resulting in a unique alpha mask for each one. By default, these occlusion mask values are computed as the Visible Difference Vegetation Index (VDVI)¹⁵, where a high value indicates vegetation and a low value indicates non-vegetation. VDVI thresholds are relatively low (e.g. T=0.025-0.115).

Supplementary Data

The following datasets are available at: https://doi.org/10.5281/zenodo.17646110

- **Data S1. Data for Figure 1.** This dataset contains the images, poses, and parameters for the RGB and NIR recordings used for Fig. 1 in the main text. Use Software S1 to load this data and compute the SA integral images.
- **Data S2. Data for Figure S3.** This dataset contains the images, poses, and parameters for the rotation, horizontal shift, and diagonal shift peering motions used for Fig. S3. Use Software S1 to load this data and compute the SA integral images.
- **Data S3. Data for Figure S4.** This dataset contains the images, poses, and parameters for the additional reasoning examples used for Fig S4. Use Software S1 to load this data and compute the SA integral images.
- **Data S4. Data for Figure S5.** This dataset contains the images, poses, and parameters for the NIR recordings used for Fig. S5. Note, that the dataset for the RGB recordings is Data S1. Use Software S1 to load this data and compute the SA integral images.

References:

- 11. I. Kurmi, D. C. Schedl, O. Bimber, Fast automatic visibility optimization for thermal synthetic aperture visualization, *IEEE Geosci. Remote Sens. Lett.***18**, 836-840 (2020). https://doi.org/10.1109/LGRS.2020.2987471
- 12. J. L. Schönberger, J. -M. Frahm, Structure-from-Motion Revisited, in *Proceedings of the 2016 IEEE Conference on Computer Vision and Pattern Recognition* (CVPR, 2016), pp. 4104-4113. https://doi.org/10.1109/CVPR.2016.445
- 13. B. Mildenhall ,P. P. Srinivasan ,M. Tancik ,J. T. Barron ,R. Ramamoorthi ,R. Ng, NeRF: Representing Scenes as Neural Radiance Fields for View Synthesis, *Commu. ACM* **65**, 99 106 (2021). https://doi.org/10.1145/3503250
- 14. J. Wang, M. Chen, N. Karaev, A. Vedaldi, C. Rupprecht, D. Novotny, VGGT: Visual Geometry Grounded Transformer, In *Proceedings of the Computer Vision and Pattern Recognition Conference* (2025), pp. 5294-5306.
- 15. J. Xue, B. Su, Significant Remote Sensing Vegetation Indices: A Review of Developments and Applications. *J. Sens.* **2017**,1353691 (2017).https://doi.org/10.1155/2017/1353691
- 16. Z. Li, X. Wu, H. Du, F. Liu, H. Nghiem, G. Shi, A Survey of State of the Art Large Vision Language Models: Alignment, Benchmark, Evaluations and Challenges, in *Proceedings of the 2025 IEEE/CVF Conference on Computer Vision and Pattern Recognition Workshops* (CVPRW, 2025), pp. 1578-1597. https://doi.org/10.1109/CVPRW67362.2025.00147